Differences between atomically-dispersed and particulate Pt supported catalysts on synergistic photothermocatalytic oxidation of VOCs from cooking oil fumes

Ying Feng, Zhiwei Wang, Mengwei Hua, Yuxi Liu, Lin Jing, Lu Wei, Zhiquan Hou, Xun Wang, Xiaohui Yu, Linke Wu, Yunpeng Jiang, Jiguang Deng [*], Hongxing Dai [*]

Beijing Key Laboratory for Green Catalysis and Separation, Key Laboratory of Beijing on Regional Air Pollution Control, Key Laboratory of Advanced Functional Materials, Education Ministry of China, Department of Environmental Chemical Engineering, Faculty of Environment and Life, Beijing University of Technology, Beijing 100124, China

ARTICLE INFO

ABSTRACT

The control of volatile organic compounds (VOCs) from cooking oil fumes via synergic photothermocatalytic oxidation not only saves energy, but also helps to reduce carbon emissions. Differences between the copper oxide−ceria (CC) supported atomically-dispersed (Pt_1/CC) and particulate Pt (Pt_{NPs}/CC) on photo-thermocatalytic heptane oxidation were investigated. The conversion efficiency at 170 °C of heptane oxidation over the Pt_1/CC catalyst was 55% higher than that over the Pt_{NPs}/CC catalyst. Pt_{NPs}/CC showed a larger capacity of heptane adsorption, but limited amounts of the adsorbed oxygen and active surface lattice oxygen species were difficult to completely oxidize the over-adsorbed heptane. Heptane and its intermediates gradually accumulated at the active sites, resulting in poor catalytic activity and stability. However, Pt_1/CC possessed a strong electron donating ability due to its unique coordination unsaturated sites and electron structure, which was conducive to oxygen activation. This allowed rapid conversion of heptane and intermediates, accelerating oxidation of the adsorbed heptane to CO_2 and H_2O. The complete oxidation of 500 ppm heptane was basically achieved at 190 °C and an optical power density of 300 mW/cm².

1. Introduction

There are a lot of volatile organic compounds (VOCs) in the exhaust gas of cooking oil fumes [1], which becomes one of the main air pollution sources in addition to industrial and mobile exhaust emissions. Since there are more than 200 kinds of VOCs, containing a large number of alkanes, aromatic hydrocarbons, and oxygen-containing organic compounds [2,3], traditional treatment methods are difficult to eliminate VOCs from cooking oil fumes. Thermocatalytic oxidation possesses the advantages of wide treatment ranges, high elimination efficiencies, and less secondary pollution [4]. However, it requires heat converted from fuels to drive the reaction. Burning fuels causes large CO_2 emissions, thus exacerbating the greenhouse effect [5,6]. China has made a solemn commitment to carbon-dioxide-emission peak by 2030 and gradually decline thereafter [7], therefore, it is urgent to develop cleaner catalytic VOCs removal technologies. The technology of synergistic photothermocatalytic oxidation [8,9] utilizes heating to provide initial power for chemical reactions within the low temperature range, and uses photoexcitation catalyst to save energy. This results in a better catalytic action than photo- or thermo-catalysis alone. Synergistic photothermocatalysis has been extensively studied in catalytic degradation of VOCs [10], catalytic oxidation of CO [11,12], catalytic hydrogen production [13], catalytic methanation or methanolation of CO_2 [14, 15], etc. Semiconductor oxide-supported noble metal catalysts have been widely used because of their excellent thermocatalytic activity and photoresponse [16].

Researchers are working to develop efficient and stable noble metal catalysts. The structure−property relationship is one of the key fundamental points in catalytic reactions. The sensitivity of most catalytic reactions to the size-dependent structures of noble metal active sites ranging from single atoms, clusters to nanoparticles (NPs) is still elusive [17–19]. For the Pt/TiO₂ catalysts with the average Pt NPs sizes of 1.3, 1.9, and 3.0 nm for toluene oxidation, the medium size of 1.9 nm showed the most outstanding catalytic activity. This was due to the large

toluene adsorption capacity and amount of surface adsorbed oxygen (O_{ads}) species [20]. Since the concept of "single atom catalysis" (SACs) was proposed [21], the applications of Pd, Ru, Cu, Co, and other single-atom catalysts in the elimination of VOCs [22–24] have become a new frontier in heterogeneous and environmental catalysis. It is obvious that the atomic dispersion as an effective means to change metal availability and electronic properties greatly regulates catalytic performance of the materials. The studies on the use of single-atom Pt catalyst for the removal of VOCs in the field of photo- or thermo-catalysis were widely reported. It has been documented from the perspective of photocatalysis that the single atoms embedded in the light-trapping semiconductor support could change the bandgap width, adjust the light absorption behavior and charge transfer [25,26]. From the point of view of thermocatalysis, the high surface free energy and unsaturated coordination environment allow the isolated metals to act as chemisorption sites for oxygen, which can promote molecular oxygen activation [27, 28]. However, the application of the atomically-dispersed catalysts for the synergistic photothermocatalytic oxidation of VOCs has been rarely reported.

Our research group's preliminary work revealed that photo-and thermo-catalysis produced synergistic effects via the reactive oxygen species (ROSs) [29–32]. The differences and causes between the atomically-dispersed and supported particulate Pt catalysts in synergistic photothermocatalytic reactions have not been well understood. Herein, we used the VOCs (heptane, hexanal or toluene) with high contents from cooking oil fumes as probe molecules, and introduced 20 vol% water vapor to the reaction system to investigate catalytic performance of the atomically-dispersed and supported particulate Pt catalysts. The optical properties, redox ability, and heptane adsorption capacity of the two catalysts were measured to find the reason for their different catalytic behaviors. Finally, a photothermocatalytic pathway for heptane oxidation was proposed. The present work provides ideas for the research and development of highly efficient catalysts for elimination of the VOCs from cooking oil fumes.

2. Experimental

2.1. Catalyst preparation

The procedures for the preparation of the catalysts were described in the Supplementary material. The actual loadings of Cu and Pt in the catalysts were determined by the inductively coupled plasma−atomic emission spectroscopy (ICP−AES) technique, as listed in Table S1.

2.2. Catalyst characterization

Physicochemical properties of the catalysts were characterized by X-ray diffraction (XRD), scanning transmission electron microscopy (STEM), aberration-corrected high-angle annular dark field−scanning transmission electron microscopy (HAADF−STEM), N_2 adsorption−desorption measurements (Brunauer−Emmett−Teller, BET), X-ray photoelectron spectroscopy (XPS), photoluminescence (PL) spectroscopy, electron paramagnetic resonance (EPR), photoelectrochemical (PEC) measurements, ultraviolet−visible−infrared spectroscopy (UV−vis−IR), O_2 or VOC temperature-programmed desorption (O_2- or VOC-TPD), hydrogen temperature-programmed reduction (H_2-TPR), VOC temperature-programmed oxidation (TPO), thermal desorption−online gas chromatography/mass spectrometry (TD−GC/MS), in situ diffuse reflectance infrared Fourier transform spectroscopy (in situ DRIFTS), and X-ray absorption spectra (XAS) including X-ray absorption near-edge structure (XANES) and extended X-ray absorption fine structure (EXAFS).

2.3. Catalytic activity evaluation

Synergistic photothermocatalytic oxidation of VOCs (heptane,

toluene or hexanal) over the catalysts were conducted in a ($12 \times 12 \times 1$ mm^3) tubular fixed-bed reactor at atmospheric pressure. Simulated light was shone onto the catalyst through the one-sided window of the furnace form Xenon lamp, and the thermocouple was placed on the surface of the catalyst to measure the reaction temperature. The optical wavelengths (λ) range and optical power density were 320–2500 nm and 300 mW/cm^2, respectively. The real optical power density was measured by an optical power meter (PM100D + S425C, Thorlabs). 0.1 g of the catalyst (40 −60 mesh) was loaded in the reactor. The reactant mixture stream was (500 ppm VOC + 20 vol% O_2 + N_2 (balance)). The total flow rate was 33.3 mL/min and the gas hourly space velocity (GHSV) of ca. 20,000 mL/(g h). The detailed characterization procedures are provided in the Supplementary material.

3. Results and discussion

3.1. Synthesis process and structure analysis

As shown in Fig. 1A, an appropriate amount of $Cu(NO_3)_2 \bullet 2 H_2O$ was added to the hydrothermally synthesized CeO_2 to form the $CuO−CeO_2$ support (CC). According to the literatures [33,34], the CC supported atomically-dispersed Pt (Pt_1/CC) catalyst was prepared by in situ icing-assisted photoreduction, and the CC supported particulate Pt (Pt_{NPs}/CC) catalyst was prepared by the ethylene glycol (EG) reduction method. XRD patterns of the Pt_1/CC and Pt_{NPs}/CC samples are shown in Fig. S1. The diffraction peaks at $2\theta = 28.7°, 33.1°, 47.5°, 56.3°, 59.1°, 69.3°, 76.5°$, and $78.8°$ were attributed to the fluorite-type cubic CeO_2 phase. In addition, the diffraction peaks at $2\theta = 35.2°$ and $38.5°$ were also observed, which were due to the (002) and (111) crystal planes of CuO. The presence of CuO may be caused by high temperature calcination [35]. The characteristic diffraction peaks of the Pt phase were not recorded in the two samples, which was due to the low Pt content and uniform Pt dispersion. Fig. 1B−I presents SEM and TEM images of the Pt_1/CC, Pt NPs, and Pt_{NPs}/CC samples. It can be seen that the Pt/CC samples exhibited a cube block structure (the side lengths were in the range of 5.6–11.9 nm), and the diameters of Pt NPs prepared by the EG reduction method were 2.3 − 7.2 nm. Through the literature comparison [29], we know that the added amount of CuO will affect morphology of the $CuO−CeO_2$ support. When the content of Cu increased to 10.32 wt%, the sample morphology changed from rod to cubic block.

The Pt distribution in Pt_{NPs}/CC and Pt_1/CC samples was characterized by in situ CO DRIFTS technique. As shown in Fig. 2A and B, after CO was adsorbed in a saturation state on the Pt_1/CC and Pt_{NPs}/CC surface, N_2 was used to purge for 30 min, leaving the absorption band of CO adsorbed at the Pt site. The absorption band at 2085 cm^{-1} appeared on the Pt_{NPs}/CC sample, which was attributed to CO adsorption on the Pt NPs. A linear absorption band with a wavenumber of 2109 cm^{-1} appeared on the Pt_1/CC catalyst, which was ascribed to the linearly bonded CO at the atomically-dispersed Pt site [36]. Fig. 2C, D, and S2 shows HAADF−STEM images of the Pt_1/CC sample, since the relative atomic weight of Pt is similar to that of Ce, the single-atom distribution of Pt was not apparently observed. However, the bright spots of the uniformly dispersed Pt atoms could still be seen [37]. Shown in Fig. 2E are the EDS elemental mappings of Pt_1/CC, from which one can see that the Pt element was evenly distributed in the Pt_1/CC sample. Fig. 2F is the Fourier transforms of EXAFS at the Pt L_3-edge spectra of the Pt_1/CC and standard samples. The fitting results are shown in Fig. 2G and Table S2. The results showed that Pt−Pt bond was not detected in the Pt_1/CC catalyst, and its Pt−O bond length (2.00 ± 0.02 Å) was similar to the Pt−O bond in the standard PtO_2, proving that the atomically-dispersed Pt existed on the CC surface in the form of a Pt−O bond. Fig. 2H shows XANES spectra of the Pt_1/CC sample. Compared with the standard Pt foil, $PtCl_2$, and PtO_2 samples, the peak of Pt_1/CC was between those of $PtCl_2$ and PtO_2, indicating that the valence state of Pt was between $2 +$ and $4 +$, which was the same as the XPS results (Fig. S3). Those results prove that the atomically-dispersed and particulate Pt supported
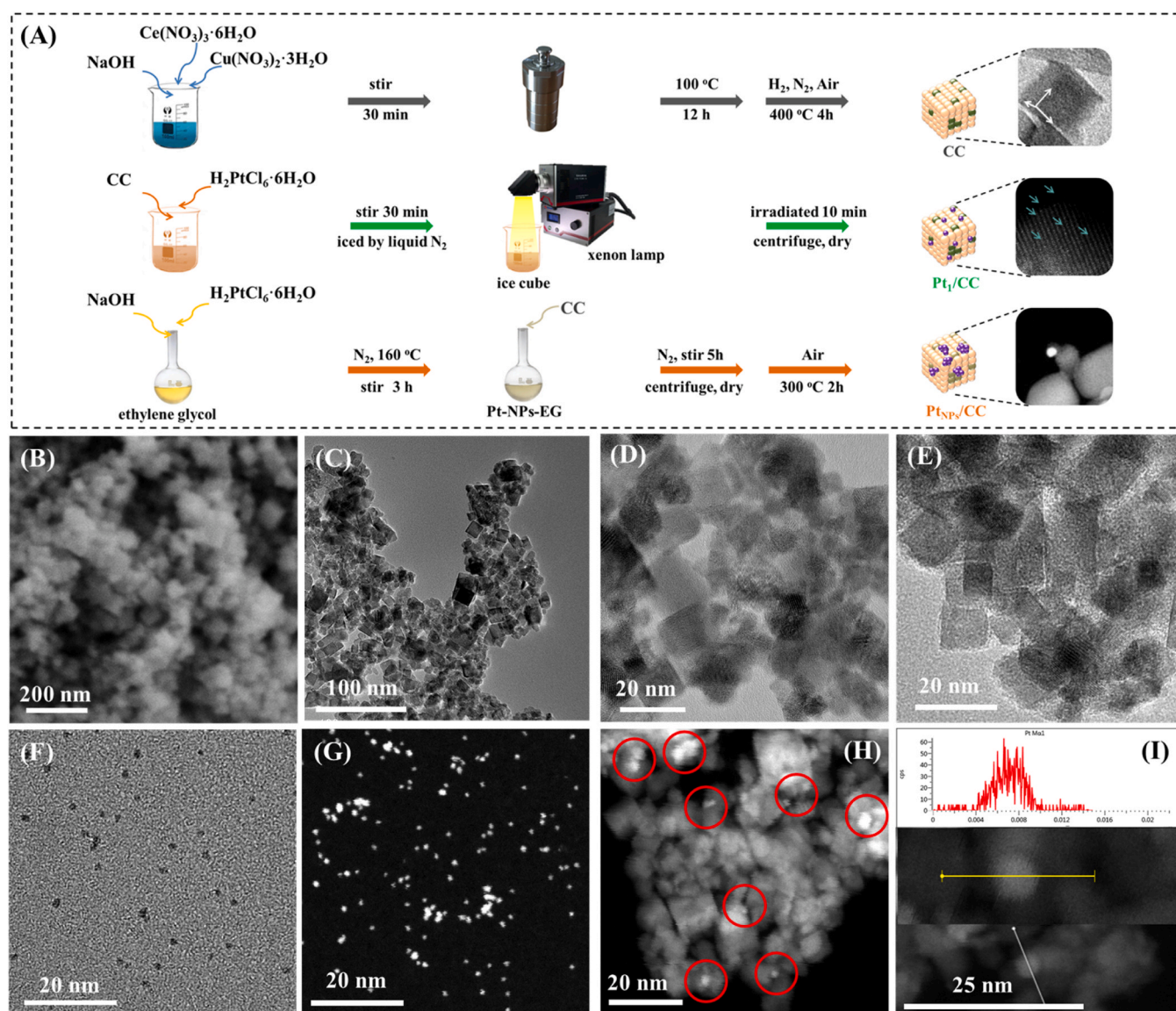
Fig. 1. (A) Schematic illustration of the procedures for the synthesis of the CC, Pt$_1$/CC, and Pt$_{NPs}$/CC samples, (B) SEM images of Pt$_1$/CC, and TEM images of (C−E) Pt$_1$/CC, (F, G) Pt nanoparticles, and (H, I) Pt$_{NPs}$/CC.

catalysts were successfully prepared. When Pt species were loaded on the pure CeO$_2$ or CuO support, homogenous single-atom Pt could not be obtained (Fig. S4). It was proved that the introduction of CuO to CeO$_2$ was beneficial for the anchoring of single-atom Pt.

3.2. Synergistic photothermocatalytic VOCs oxidation performance

As shown in Fig. 3A, heptane, as one of the representative VOCs from cooking oil fumes, was used to evaluate photothermocatalytic activities of the as-obtained samples under the conditions of 500 ppm heptane and GHSV = 20,000 mL/(g h). The full-spectrum simulated sunlight power density of 300 mW/cm^2 was chosen in the present work since the Pt$_1$/CC catalyst showed the satisfactory catalytic performance under the irradiation of the light with an optical power density of 300 mW/cm^2 (Figs. S5 and S6). CuO possessed the worst photothermocatalytic activity for heptane oxidation, but the performance of CuO−CeO$_2$ was slightly improved. We speculate that this may be related to the increase in surface area (Table S1). The loading of Pt was beneficial for improving the photothermocatalytic activity of heptane oxidation. When the actual Pt content was 0.20 wt%, the catalyst exhibited an optimal

photothermocatalytic oxidation performance (the 0.20Pt$_1$/CC is referred to Pt$_1$/CC in the following sections). The temperature required for 90% conversion of heptane over the Pt$_1$/CC catalyst was about 42 $^\circ$C lower than that over the CC support (statistical data are listed in Table S3). The photothermocatalytic heptane oxidation efficiencies of the Pt$_1$/CC and Pt$_{NPs}$/CC catalysts were evaluated. It can be seen from Fig. 3B that heptane conversions over Pt$_1$/CC were higher than those over Pt$_{NPs}$/CC. In the range of 140–180 $^\circ$C, heptane conversion increased rapidly. In particular, at 170 $^\circ$C, the heptane conversion over the Pt$_1$/CC and Pt$_{NPs}$/CC catalysts reached a huge difference of 55%. At 190 $^\circ$C, heptane was basically completely converted into CO$_2$ over Pt$_1$/CC. The VOCs with high concentrations from cooking oil fumes are alkanes, aldehydes, and ketones, accompanied by a certain quantity of aromatics [1]. Therefore, we tested the Pt$_1$/CC and Pt$_{NPs}$/CC catalysts for the photothermocatalytic oxidation of toluene and hexanal, respectively. The reaction conditions and VOCs concentration were the same as that of photothermocatalytic heptane oxidation. The results are shown in Fig. S7. Obviously, the atomically-dispersed Pt catalyst still showed better activity than the Pt$_{NPs}$/CC catalyst. When the temperature reached 170 $^\circ$C, 500 ppm hexanal was basically completely
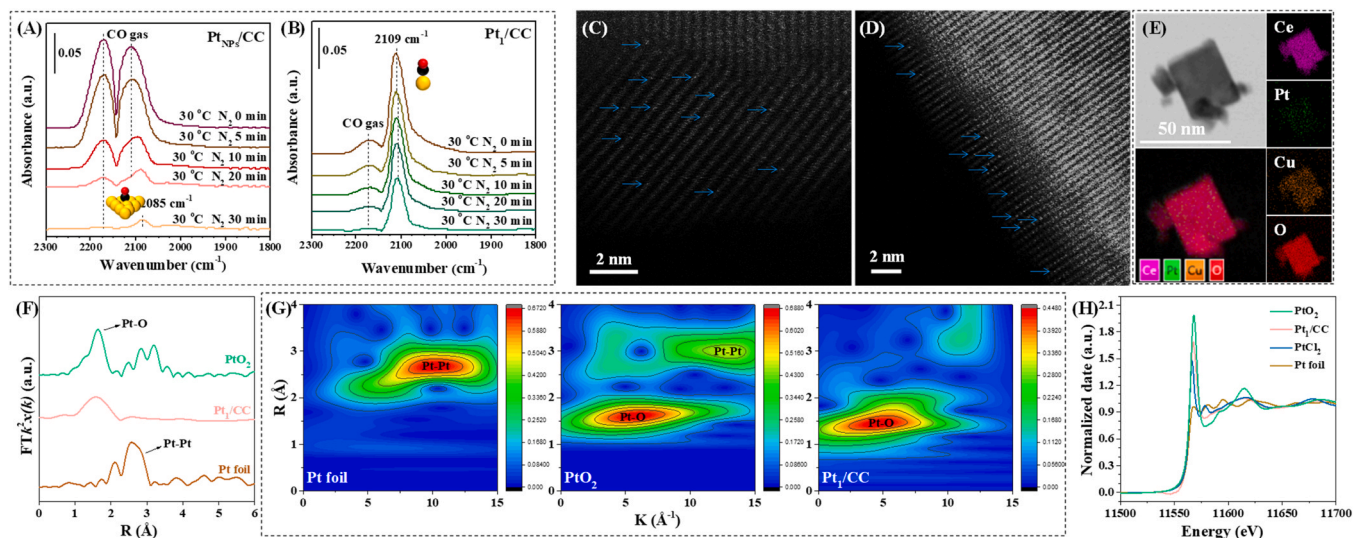
Fig. 2. In situ CO DRIFTS spectra of (A) Pt_{NPs}/CC and (B) Pt_1/CC, (C, D) HAADF−STEM images of Pt_1/CC, and (E) EDS elemental mappings of Pt_1/CC, (F) Fourier transforms of EXAFS at the Pt L_3-edge spectra, (G) wavelet transforms for Pt L_3-edge, and (H) Pt L_3-edge XANES spectra of Pt_1/CC.
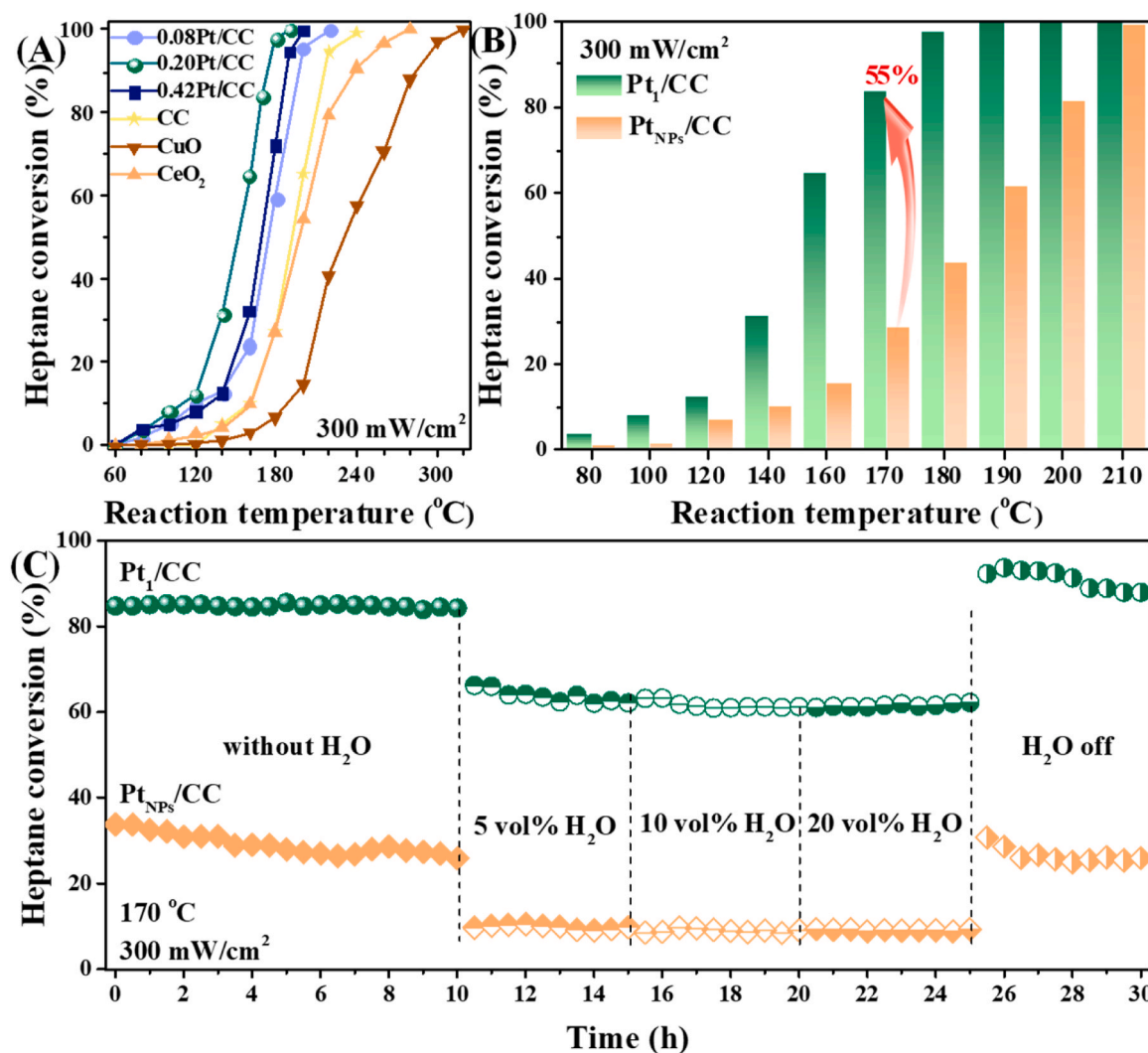

Fig. 3. (A) The relationship between temperature and heptane conversions over $0.08Pt_1/CC$, $0.20Pt_1/CC$, $0.42Pt_1/CC$, CC, CuO, and CeO_2, (B) heptane conversion over the Pt_1/CC and Pt_{NPs}/CC catalysts as a function of temperature, and (C) catalytic stability and effect of 5, 10 or 20 vol% H_2O on catalytic activity of the Pt_1/CC and Pt_{NPs}/CC sample. Reaction conditions: 500 ppm heptane + 20 vol% O_2 + N_2 (balance), GHSV = 20,000 mL/(g h), simulated solar illumination (λ = 320–2500 nm), and optical power density = 300 mW/cm^2.

transformed, and 500 ppm toluene was basically completely transformed at ca. 210 °C. The Pt$_1$/CC catalyst showed the positive photothermocatalytic VOCs oxidation performance.

The photothermocatalytic heptane oxidation stability at 170 °C of the two catalysts was compared, as shown in Fig. 3C. After 10 h of the continuous photothermocatalytic oxidation, the conversion of heptane over the Pt$_1$/CC catalyst remained unchanged, while that over Pt$_{NPs}$/CC significantly declined from 33 to ca. 25%. The stability of the atomically-dispersed Pt catalyst was better than the particulate Pt catalyst. The specific reasons need to be further explored. It cannot be ignored that cooking oil fumes often contain a large amount of H$_2$O vapor [2]. A number of previous studies have shown that the presence of H$_2$O is not conducive to the elimination of VOCs by the thermocatalytic oxidation [38,39]. Compared with dark conditions, however, the improvement in synergistic photothermocatalytic oxidation activity was related to the increase in the ROSs on the catalyst surface under light illumination. The addition of photogenic •OH and •O$_2^-$ further accelerated oxidation of the intermediates, thus speeding up the reaction process. The main source of •OH was believed to be from the H$_2$O adsorbed on the catalytic surface. Theoretically, the existence of H$_2$O was conducive to the photothermal VOCs oxidation [40], so the conversion of heptane over Pt$_1$/CC and Pt$_{NPs}$/CC in the presence of H$_2$O was explored. As shown in Fig. 3C, the influence of 5, 10 or 20 vol% water vapor on catalytic performance of Pt$_1$/CC and Pt$_{NPs}$/CC was investigated at 170 °C for 15 h of reaction. For the Pt$_1$/CC catalyst, when 5 − 20 vol% water vapor was introduced to the reaction system after 10 h of heptane oxidation, heptane conversion decreased from 83% to 61% and basically remained stable. For the Pt$_{NPs}$/CC catalyst, heptane conversion decreased to 9% after water vapor addition. After the H$_2$O was cut off, heptane conversions over both catalysts first increased slightly and then decreased to their initial levels in the absence of water vapor during the 10-h reaction process. It was shown that a water content of 5 − 20 vol% leaded to a reversible deactivation of the heptane oxidation over the two catalysts. Perhaps only a small amount of H$_2$O acted as a hydroxyl source [41]. The Pt species on the surface of the "Pt$_1$/CC used" catalyst after 30-h stability and water resistance tests were mainly in the form of single atoms (Fig. S8), which further proved that this catalyst possessed a good structural stability.

3.3. Optical properties of Pt$_1$/CC and Pt$_{NPs}$/CC

The optical properties of the Pt$_1$/CC and Pt$_{NPs}$/CC catalysts were investigated. Excellent light absorption capacity is one of the important factors for the synergistic photothermal catalyst. The UV−vis−IR spectroscopic technique was used to characterize the optical absorption capacity of the sample. As shown in Fig. 4A, both samples exhibited light absorption capacity in the wavelength range of 200–2400 nm. The light absorption of the two catalysts was basically indistinguishable. Notably, the Pt$_1$/CC sample exhibited a stronger infrared absorption ability. The

natural sunlight spectrum consists of (5% UV light + 43% visible light + 52% infrared light). The light absorption of a catalyst in the infrared light range can effectively improve utilization of the solar energy. The PL spectrum was used to evaluate the separation ability of photon-generated charge carriers. As shown in Fig. 4B, the PL intensity of the band at 468 nm for Pt$_1$/CC was slightly lower than that for Pt$_{NPs}$/CC, indicating that the charge separation efficiency of Pt$_1$/CC was better than that of Pt$_{NPs}$/CC. The photocurrent-time curves of the samples are shown in Fig. 4C. Compared with Pt$_{NPs}$/CC, Pt$_1$/CC showed a higher photocurrent response in 5 on/off lamp cycles. Fig. 4D shows the EIS test results. The arc radium of the Pt$_1$/CC electrode was slightly smaller than that of the Pt$_{NPs}$/CC electrode. In general, when Pt NPs were reduced to single atoms, the interaction between Pt and CC was amplified. As a light trapping medium, the support was more closely bound to the atomically-dispersed Pt, thus shortening the charge transfer distance. Therefore, the recombination and relaxation of the photogenerated e$^-$ and h$^+$ were effectively inhibited during the migration of the photogenerated carriers from the support to the single-atom Pt sites, which means that utilization efficiency of the photogenerated carriers is improved [42–44]. Overall, the optical properties of Pt$_1$/CC were better than those of Pt$_{NPs}$/CC, but the difference was not very pronounced. Therefore, we speculated that the above differences were not the main reasons for the differences in catalytic properties of the two catalysts.

3.4. Redox property and surface oxygen species

In catalytic reactions, redox properties as well as adsorption and activation of molecular oxygen are important [45]. Fig. 5A and B shows H$_2$-TPR and O$_2$-TPD profiles of the Pt$_1$/CC and Pt$_{NPs}$/CC samples, respectively. It can be seen from Fig. 5A that both samples showed three reduction peaks: The peaks below 200 °C belonged to reduction of the surface CuO and Pt$^{\mathcal{E}+}$ species ($\mathcal{E}$ = 2 or 4) (Fig. S3) and/or the removal of the surface O$_{ads}$; and the peaks below 500 °C and at ca. 770 °C were attributed to reduction of the surface Ce^{4+} to Ce^{3+} species as well as removal of the surface lattice oxygen (O$_{latt}$) species, and/or reduction of even bulk Ce^{4+} to Ce^{3+} species as well as removal of the bulk lattice oxygen [46], respectively. The reduction peak of Pt$_1$/CC catalyst was shifted to a lower temperature compared to Pt$_{NPs}$/CC catalyst, which was consistent with what was revealed by Fig. 5B. The loading of the atomically-dispersed Pt decreased the desorption temperature of O$_{ads}$ from the sample surface, and the strong electron donating capability of Pt favored the adsorption and activation of O$_2$. The O 1 s XPS spectra (Fig. 5C) could be divided into three components, assignable to the O$_{latt}$ species at binding energy (BE) = 529.2 eV, the O$_{ads}$ species at BE = 531.1 eV, and the surface hydroxyl or carbonate species at BE = 533.1 eV [47]. The O$_{ads}$/O$_{latt}$ values of 0.36 and 0.30 for Pt$_1$/CC and Pt$_{NPs}$/CC samples, respectively, were consistent with their catalytic activity changing trend.

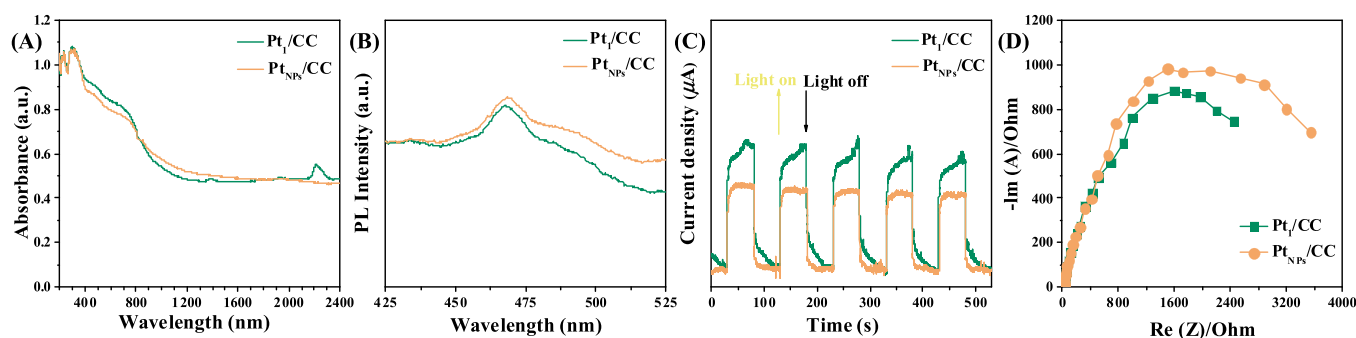According to the Wigner's spin selection rule, activation of the

Fig. 4. (A) UV−vis−IR diffuse reflectance spectra, (B) PL spectra with excitation by a Xe lamp (wavelength λ = 280 nm) of the Pt$_1$/CC and Pt$_{NPs}$/CC samples, (C) amperometric current−time curves of the Pt$_1$/CC and Pt$_{NPs}$/CC electrodes under on-off simulated sunlight exposure pulse of 100 s with a constant bias of 0.2 V vs. Ag/AgCl electrode, and (D) EIS Nyquist plots of the Pt$_1$/CC and Pt$_{NPs}$/CC samples.
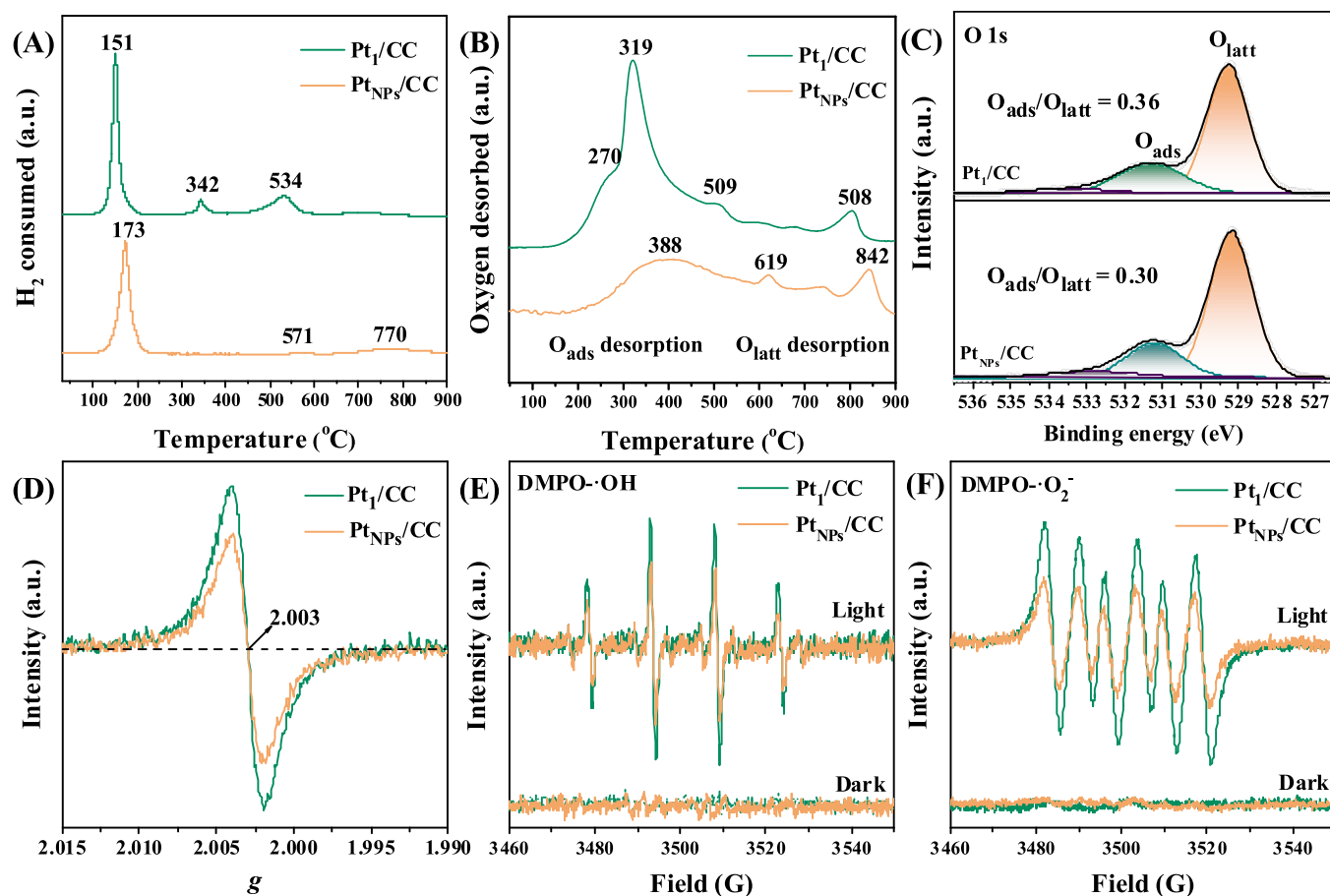
Fig. 5. (A) H_2-TPR and (B) O_2-TPD profiles, (C) O 1 s XPS spectra, (D) ESR spectra, and (E) DMPO–•OH and (F) DMPO–•O_2 EPR spectra of the Pt_1/CC and Pt_{NPs}/CC catalysts.

ground-state O_2 into ROSs is beneficial for the oxidation reaction [48]. Electron paramagnetic resonance (EPR) technique confirmed the oxygen vacancy (V_O^+) on the two catalysts, as shown in Fig. 5D. The signal near $g = 2.003$ was due to the V_O^+ of unpaired electrons caused by the sample surface defects [49]. The surface of Pt_1/CC possessed a higher oxygen vacancy concentration than that of Pt_{NPs}/CC, which helped to adsorb oxygen molecules and produced more ROSs. The differences will also lead to the different concentration of free radicals produced by the two catalysts during the photothermocatalytic process. Indirect DMPO-assisted EPR was used to evaluate hydroxyl and superoxide radical production on Pt_1/CC and Pt_{NPs}/CC under light irradiation or in darkness (Fig. 5E and F). After 10 min of illumination ($\lambda = 200$–2400 nm), both samples showed characteristic peaks of the •OH and •O_2^- species, and no signals were observed under the dark condition. Compared with the Pt_{NPs}/CC sample, the Pt_1/CC sample showed more obvious EPR signals, indicating that more amounts of the •OH and •O_2^- species were generated on the single-atom catalyst under the light irradiation.

The above differences in oxygen species activation behavior led to the differences in catalytic performance of the atomically-dispersed and particulate Pt samples. It has been shown that O_2 activation on the catalyst surface was largely dependent upon its electronic, geometric, and energy properties. Activation of O_2 at the sites with low coordination numbers is much easier than activation at the sites with high coordination numbers [50]. Zhang et al. reported that the atomically dispersed catalysts showed higher activities and selectivity for the oxidation of alcohols than the particulate counterparts, since the maximum exposure of the interfacial sites in SACs promoted the activation of O_2 molecules [51].

3.5. Heptane-TPD and TPO behaviors

Catalytic reaction processes are well known to take place via the pathway of internal/external diffusion → chemisorption of VOCs to form active intermediates → formation and desorption of products. The adsorption of VOCs on the active sites is an important part of the catalytic reaction. The adsorption capacity of VOCs depends on the structure of the active site, which is affected by several factors (e.g., size, shape, composition, and coordination environment [52]). We used the VOC-TPD technique to investigate the adsorption of heptane on the two catalysts at room temperature under the simulated sunlight illumination for 4 h. Their profiles are shown in Fig. 6. The heptane ($m/z = 71$) desorption peaks of the Pt_1/CC and Pt_{NPs}/CC catalysts appeared at 389 and 385 °C (Fig. 6A), respectively. There were desorption peaks assignable to intermediate products ($m/z = 43$, such as butanone) of the two catalysts at corresponding temperatures (Fig. 6B), which were attributed to the physical adsorption and chemical adsorption of heptane and intermediates on the catalysts [53]. Fig. 6C and D shows the desorption peaks of CO_2 ($m/z = 44$) and CO ($m/z = 28$). Desorption of heptane from Pt_1/CC was less than that from Pt_{NPs}/CC, whereas desorption of butanone, CO, and CO_2 was more than that from Pt_{NPs}/CC. This indicated that the Pt_{NPs}/CC catalyst possessed a larger VOCs adsorption capacity. But the oxygen activity on Pt_{NPs}/CC was not enough, so the photothermal oxidation capacity was insufficient. To further confirm the above conclusions, O_2 was introduced into the heptane desorption process. At a heating ramp of 10 °C/min, the catalysts and surface adsorbed heptane were oxidized with O_2. As shown in Fig. 6E, the Pt_{NPs}/CC catalyst also exhibited a larger heptane desorption capacity. The difference was that the introduction of oxygen promoted
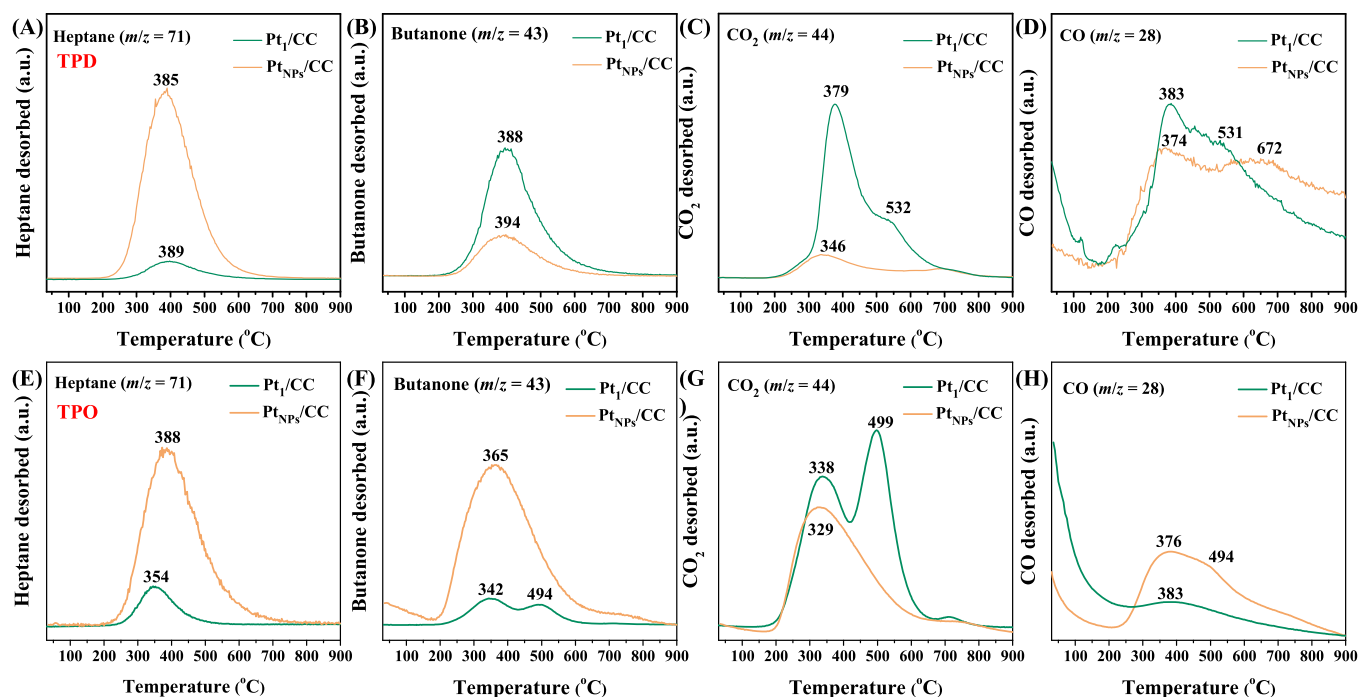
Fig. 6. (A, E) heptane, (B, F) hexanal, (C, G) CO₂, and (D, H) CO desorption in the heptane-TPD and heptane-TPO profiles of Pt₁/CC and Pt$_{NPs}$/CC, respectively.

the oxidation of heptane on the catalyst surface. The amount of incomplete oxidation products such as butanone and CO produced on Pt$_{NPs}$/CC catalyst was higher than that on Pt₁/CC catalyst (Fig. 6F, H), and the gap between the amount of CO₂ produced (Fig. 6G) on Pt$_{NPs}$/CC catalyst and that on Pt₁/CC catalyst was also reduced. According to the literature [47], it was difficult for the limited amount of the adsorbed oxygen and active lattice oxygen species to completely react with the over-adsorbed heptane. Heptane and its intermediates gradually accumulate at the active sites, resulting in poor catalytic activity and stability (Fig. 3). The Pt₁/CC catalyst possessed a strong electron-donating ability and redox property (Fig. 4), which accelerated oxidation of the adsorbed heptane to CO₂ and H₂O via further conversion of the intermediate products [46]. It can be inferred that the main reasons for the differences in the performance of synergistic photothermocatalytic oxidation between the two catalysts were the oxygen activation and adsorption properties.

3.6. Possible reaction mechanism during heptane photothermal oxidation over Pt₁/CC

To determine the intermediate products that may be generated during the photothermocatalytic heptane oxidation process, the in situ DRIFTS technique was employed. The Pt₁/CC catalyst was exposed to a high concentration of a heptane (balanced with air) flow at $160 - 280$ °C to measure the vibration bands of the intermediate products in the oxidation of heptane. The bands near 1025, 1337, 1485, and 1533 cm^{-1} were due to δ(C–H) in-plane bending vibration of alkanes. The strong absorption bands near $2879 - 2967$ cm^{-1} were attributed to the asymmetric or symmetric v(C–H) stretching vibrations [54]. The band at about 1045 cm^{-1} was assigned to the v(C–O) stretching vibrations of alcohols. The absorption bands near 1498 cm^{-1} were ascribed to the asymmetric or symmetric v(–COO–) stretching vibrations [29]. Water molecules (at 1621 cm^{-1}) were coordinated with the Pt₁/CC surface, and the bands near 3494 and 3738 cm^{-1} were owing to the v(M–OH) stretching vibrations. The band near 2356 cm^{-1} was assigned to the
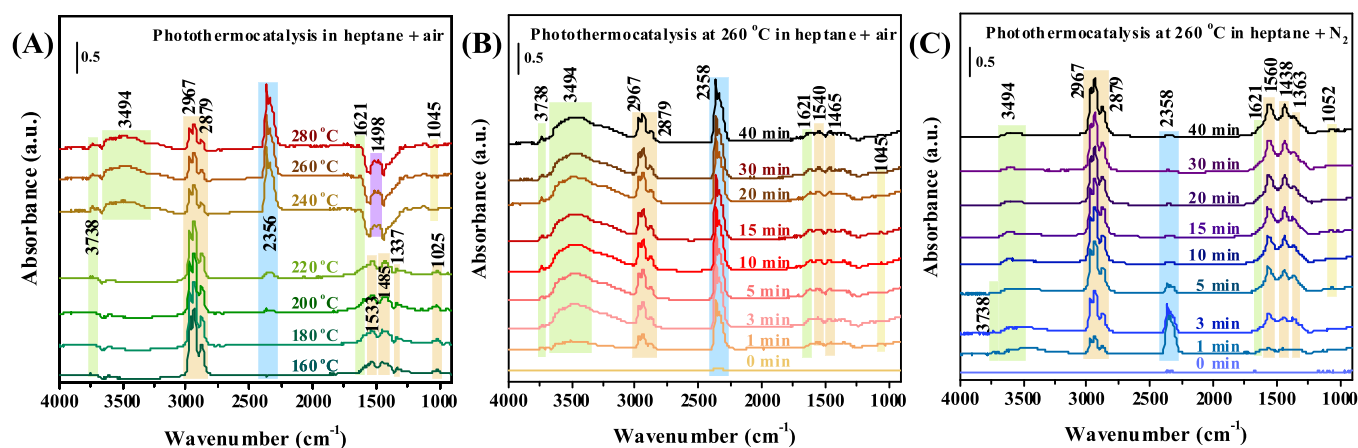

Fig. 7. In situ DRIFTS spectra of photothermocatalytic heptane oxidation for transient reactions over the Pt₁/CC catalyst in (A) heptane + air at $160 - 240$ °C, (B) heptane + air or (C) heptane + N₂ at 260 °C for 40 min.

stretching vibration of $v(C–O)$ bond from CO_2 [9].

In Fig. 7A, each curve was obtained after 15 min of the photo-thermocatalytic oxidation. With the rise in temperature, the vibration band of CO_2 at 2356 cm^{-1} gradually became obvious, and the bending and stretching vibration bands of C−H in heptane (alkane) were significantly reduced. When the temperature rose to a certain value, there were obvious vibration bands of H_2O (at 1621 cm^{-1}), −OH (at 3494 cm^{-1}), and -COO- (at 1498 cm^{-1}). This indicates that heptane gradually passes through the intermediates, eventually producing CO_2 and H_2O. Furthermore, the catalyst was exposed to a (heptane + air) or (heptane + N_2) atmosphere at 260 °C for 40 min to compare the differences in vibration bands of the intermediate products and explore whether the surface O_{ads} and subsurface O_{latt} species participated in the activation and oxidation processes of heptane. In Fig. 7B, the intermediate products vibration bands were recorded in the aerobic environment. In Fig. 7C, the vibration bands of heptane at 260 °C were recorded in the anaerobic environment. The position of vibration band of the intermediate products of photothermal heptane oxidation was basically the same under the different conditions. Obviously, in the presence of gas-phase oxygen, intensity of the vibration bands due to heptane first increased, then decreased, and finally remained stable. Over time, the vibration bands of −OH, H_2O, and CO_2 gradually increased, indicating the gradual oxidation of heptane. In Fig. 7C, the C−H stretching and bending vibrations of heptane (near 2879 −2967 and 1363 −1560 cm^{-1}) gradually increased, and became stable. The vibration bands representing H_2O and CO_2 obviously existed within 5 min, but then gradually decreased until they almost disappeared. This result indicates that the surface O_{ads} species are involved in the activation and elimination of heptane in the absence of gas-phase oxygen. The amounts of the O_{ads} was limited, and the catalyst would lose its activity if the oxygen species were not supplemented in time. This was consistent with the conclusion shown in Fig. 6 that heptane desorption was large but CO_2 generation was small on the Pt_{NPs}/CC catalyst.

To further understand the possible reaction pathways, the TD−GC/MS technique was employed. The spectra were obtained by desorption of heptane after 1 h adsorption at the given temperatures (corresponding to the temperatures needed for 10%, 50%, and 90% heptane conversion) under the photothermal conditions. As shown in Fig. 8, a total of 11 products besides heptane were detected: acetaldehyde (1), ethanol (2), pentane (3), butanone (4), tetrahydrofuran (5), heptane, 3-methyl (6), hexane, 3-methyl (7), 2-pentanone (8), heptane (9), octane, 2,3-dimethyl (10), pentane, 2,3-dimethyl (11), and heptanol (12). By comparing the types of intermediates at the same heptane conversion, it was found that there was no significant difference in intermediate type between the Pt_1/CC and Pt_{NPs}/CC catalysts. With the conversion of heptane, the heptane isomerization products first increased, then were oxidized, and the oxygen-containing organic compounds gradually

appeared. There was no significant difference in heptane conversion pathway between the atomically-dispersed and particulate Pt catalysts. Combining the results of GC−MS and heptane-TPD with those reported in the literature [32,55], we speculate that the general reaction pathways of heptane is as follows: *n*-heptane → isopheptane → alcohols and aldehydes → short-chain alkanes → short-chain alcohols → CO_2 and H_2O (Fig. 9).

4. Conclusions

In conclusion, compared with the Pt_{NPs}/CC catalyst, the atomically-dispersed Pt_1/CC catalyst exhibited a strong synergistic photo-thermocatalytic heptane oxidation ability. On the one hand, the Pt_1/CC catalyst was more favorable for the photogenerated charge carriers separation and migration; on the other hand, the specific coordination unsaturated sites and unique electronic structure of Pt_1/CC rendered it to possess a strong electron-donating ability that could promote the activation of O_2 molecules. The adsorption of heptane on Pt_1/CC was smaller than that on Pt_{NPs}/CC, however, the O_2 adsorption and activation ability of Pt_1/CC was stronger, leading to the improvement in

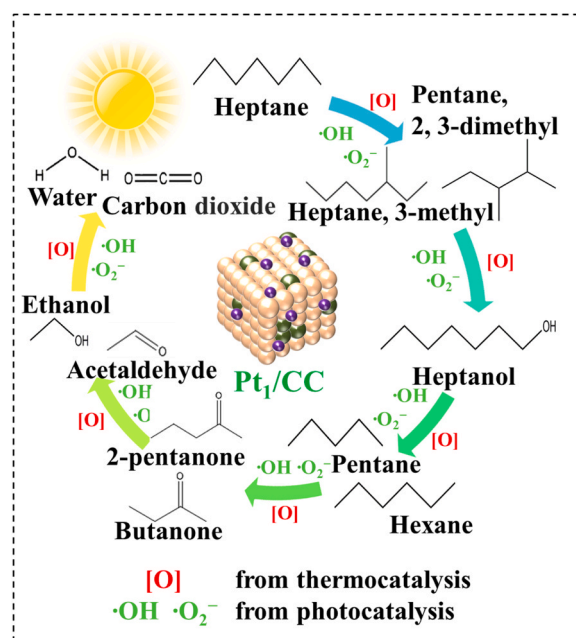**Fig. 9.** Possible mechanism of synergistic photothermocatalytic heptane oxidation over the Pt_1/CC catalyst.

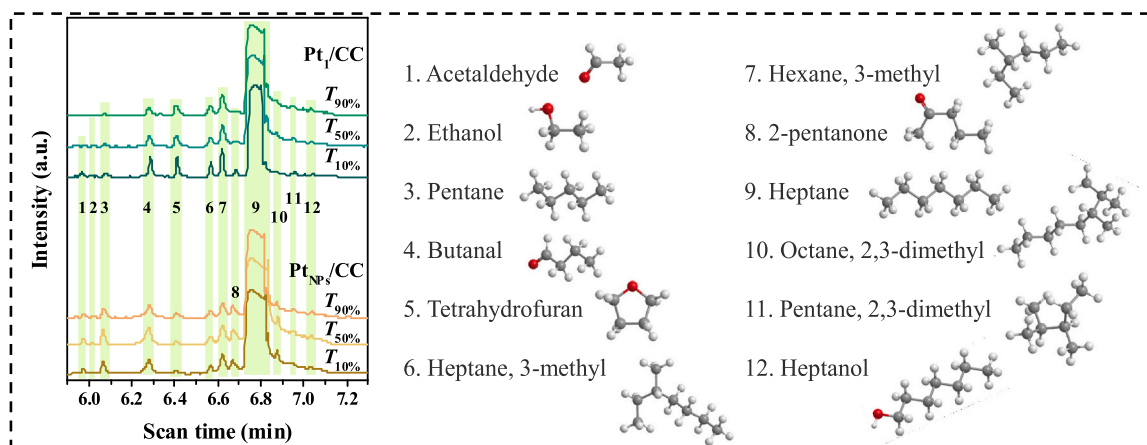**Fig. 8.** Reaction intermediates detected during the heptane photothermal oxidation process over the Pt_1/CC and Pt_{NPs}/CC catalysts at different temperatures.

heptane conversion efficiency. The Pt_1/CC catalyst possessed excellent synergistic photothermal elimination performance and H_2O resistance for the typical VOCs (e.g., heptane, toluene, and hexanal) from cooking oil fumes. After isomerization and chain-breaking, heptane was gradually oxidized to alcohols and aldehydes, and finally completely converted into CO_2 and H_2O.

Declaration of interest statement

We certify that this manuscript consists of original, unpublished work which is not under consideration for publication elsewhere. We declare no competing financial interest.

CRediT authorship contribution statement

Ying Feng: Writing – review & editing, Investigation. **Zhiwei Wang:** Investigation, Data curation. **Mengwei Hua:** Investigation, Data curation. **Yuxi Liu:** Investigation. **Lin Jing:** Investigation. **Lu Wei:** Investigation. **Zhiquan Hou:** Investigation. **Xun Wang:** Investigation, Data curation. **Xiaohui Yu:** Investigation, Data curation. **Linke Wu:** Investigation, Data curation. **Yunpeng Jiang:** Investigation, Data curation. **Jiguang Deng:** Writing – review & editing, Methodology, Supervision, Project administration. **Hongxing Dai:** Writing – review & editing, Methodology, Supervision, Project administration.

Declaration of Competing Interest

The authors declare that they have no known competing financial interests or personal relationships that could have appeared to influence the work reported in this paper.

Data Availability

Data will be made available on request.

Acknowledgements

Appendix A. Supporting information

Supplementary data associated with this article can be found in the online version at doi:10.1016/j.apcatb.2023.123116.

References

[1] H.H. Yi, Y.H. Huang, X.L. Tang, S.Z. Zhao, X.Z. Xie, Y.Y. Zhang, Characteristics of non-methane hydrocarbons and benzene series emission from commonly cooking oil fumes, Atmos. Environ. 200 (2019) 208–220.

[2] L.N. Wang, L.Y. Zhang, Z. Ristovski, X.R. Zheng, H.L. Wang, L. Li, J. Gao, F. Salimi, Y.Q. Gao, S.G. Jing, L. Wang, J.M. Chen, S. Stevanovic, Assessing the effect of reactive oxygen species and volatile organic compound profiles coming from certain types of Chinese cooking on the toxicity of human bronchial epithelial cells, Environ. Sci. Technol. 54 (2020) 8868–8877.

[3] C. Chen, Y.J. Zhao, B. Zhao, Emission rates of multiple air pollutants generated from Chinese residential cooking, Environ. Sci. Technol. 52 (2018) 1081–1087.

[4] Y. Feng, L. Wei, Z.W. Wang, Y.X. Liu, H.X. Dai, C. Wang, H.C. Hsi, E.H. Duan, Y. Peng, J.G. Deng, Boosting catalytic stability for VOCs removal by constructing PtCu alloy structure with superior oxygen activation behavior, J. Hazard. Mater. 439 (2022), 129612.

[5] M.Y. Zhang, S.M. Jordaan, W. Peng, Q. Zhang, S.M. Miller, Potential uses of coal methane in China and associated benefits for air quality, health, and climate, Environ. Sci. Technol. 54 (2020) 12447–12455.

[6] D. Nong, P. Simshauser, D.B. Nguyen, Greenhouse gas emissions vs CO_2 emissions: Comparative analysis of a global carbon tax, Appl. Energy 298 (2021), 117223.

[7] G.Y. Xu, H.Y. Dong, Z.C. Xu, N.S. Bhattarai, China can reach carbon neutrality before 2050 by improving economic development quality, Energy 243 (2022), 123087.

[8] M. Zhang, G.H. Li, Q. Li, J. Chen, E.A. Elimian, H.P. Jia, H. Hong, In situ construction of manganese oxide photothermocatalysts for the deep removal of toluene by highly utilizing sunlight energy, Environ. Sci. Technol. 57 (2023) 4286–4297.

[9] S.L. Jiang, C.H. Li, Y. Muhammad, Y. Tang, R.M. Wang, J.J. Li, J. Li, Z.X. Zhao, Z.X. Zhao, Solvent-induced fabrication of Cu/MnO_x nanosheets with abundant oxygen vacancies for efficient and long-lasting photothermal catalytic degradation of humid toluene vapor, Appl. Catal. B 328 (2023), 122509.

[10] J.W. Li, J.R. Feng, X.M. Guo, H.L. Fang, J.Y. Chen, C.R. Ma, R.C. Li, Y.Y. Wang, Z.B. Rui, Defect-band bridge photothermally activates type III heterojunction for CO_2 reduction and typical VOCs oxidation, Appl. Catal. B 309 (2022), 121248.

[11] R.R. Gui, J.W. Xiao, Y.S. Gao, Y.R. Li, T.Y. Zhu, Q. Wang, Simultaneously achieving selective catalytic reduction of NO_x with NH_3 and catalytic oxidation of CO with O_2 over one finely optimized bifunctional catalyst $Mn_2Cu_1Al_1O_x$ at low temperatures, Appl. Catal. B 306 (2022), 121104.

[12] Z.W. Liu, L.J. Niu, X.P. Zong, L. An, D. Qu, X.Y. Wang, Z.C. Sun, Ambient photothermal catalytic CO oxidation over a carbon-supported palladium catalyst, Appl. Catal. B 25 (2022), 121439.

[13] X.M. Guo, J.W. Li, Y.J. Wang, Z.B. Rui, Photothermocatalytic water splitting over $Pt/ZnIn_2S_4$ for hydrogen production without external heat, Catal. Today 402 (2022) 210–219.

[14] Y.Y. Li, C.H. Wang, M. Song, D.S. Li, X.T. Zhang, Y.C. Liu, $TiO_{2−x}/CoO_x$ photocatalyst sparkles in photothermocatalytic reduction of CO_2 with H_2O steam, Appl. Catal. B 243 (2019) 760–770.

[15] R. Fiorenza, M. Bellardita, S.A. Balsamo, L. Spitaleri, A. Gulino, M. Condorelli, L. D'Urso, S. Scirè, L. Palmisano, A solar photothermocatalytic approach for the CO_2 conversion: Investigation of different synergisms on CoO–CuO/brookite TiO_2–CeO_2 catalysts, Chem. Eng. J. 428 (2022) 131249.

[16] E.A. Elimian, M. Zhang, J. Chen, H.P. Jia, Y. Sun, J. He, Construction of Pt-$mTiO_2$/USY multifunctional catalyst enriched with oxygen vacancies for the enhanced light-driven photothermocatalytic degradation of toluene, Appl. Catal. B 307 (2022), 121203.

[17] W. Zhang, H.Z. Wang, J.W. Jiang, Z.J. Sui, Y.A. Zhu, D. Chen, X.G. Zhou, Size Dependence of Pt catalysts for propane dehydrogenation: from atomically dispersed to nanoparticles, ACS Catal. 21 (2020) 12932–12943.

[18] M. Peng, Z.M. Jia, Z.R. Gao, M. Xu, D.Y. Cheng, M. Wang, C.Y. Li, L.L. Wang, X.B. Cai, Z. Jiang, H. Jiang, N. Wang, D.Q. Xiao, H.Y. Liu, D. Ma, Antisintering Pd_1 catalyst for propane direct dehydrogenation with in situ active sites regeneration ability, ACS Catal. 12 (2022) 2244–2252.

[19] R.R. Seemakurthi, G. Canning, Z.W. Wu, J.T. Miller, A.K. Datye, J. Greeley, Identification of a selectivity descriptor for propane dehydrogenation through density functional and microkinetic analysis on pure Pd and Pd alloys, ACS Catal. 11 (2021) 9588–9604.

[20] Z.W. Wang, P.J. Ma, K. Zheng, C. Wang, Y.X. Liu, H.X. Dai, C.C. Wang, H.C. Hsi, J.G. Deng, Size effect, mutual inhibition and oxidation mechanism of the catalytic removal of a toluene and acetone mixture over TiO_2 nanosheet-supported Pt nanocatalysts, Appl. Catal. B 274 (2020), 118963.

[21] B.T. Qiao, A.Q. Wang, X.F. Yang, L.F. Allard, Z. Jiang, Y.T. Cui, J.Y. Liu, J. Li, T. Zhang, Single-atom catalysis of CO oxidation using Pt_1/FeO_x, Nat. Chem. 3 (2011) 634–641.

[22] F.K. Bi, Z.Y. Zhao, Y. Yang, W.K. Gao, N. Liu, Y.G. Huang, X.D. Zhang, Chlorine-coordinated Pd single atom enhanced the chlorine resistance for volatile organic compound degradation: mechanism study, Environ. Sci. Technol. 56 (2022) 17321–17330.

[23] Y. Chen, J. Lin, B.H. Jia, X.D. Wang, S.Y. Jiang, T.Y. Ma, Isolating single and few atoms for enhanced catalysis, Adv. Mater. 34 (2022) 2201796.

[24] C.M. Li, N. Su, H.H. Wu, C.B. Liu, G.B. Che, H.J. Dong, Synergies of adjacent sites in atomically dispersed ruthenium toward achieving stable hydrogen evolution, Inorg. Chem. 61 (2022) 13453–13461.

[25] C.M. Li, H.H. Wu, D.Q. Zhu, T.X. Zhou, M. Yan, G. Chen, J.X. Sun, G. Dai, F. Ge, H.J. Dong, High-efficient charge separation driven directionally by pyridine rings grafted on carbon nitride edge for boosting photocatalytic hydrogen evolution, Appl. Catal. B 297 (2021), 120433.

[26] C.M. Li, D.Q. Zhu, S.S. Cheng, Y. Zou, Y. Wang, C.C. Ma, H.J. Dong, Recent research progress of bimetallic phosphides-based nanomaterials as cocatalyst for photocatalytic hydrogen evolution, Chin. Chem. Lett. 33 (2022) 1141–1153.

[27] Y.R. Fang, Q. Zhang, H. Zhang, X.M. Li, W. Chen, J. Xu, H. Shen, J. Yang, C.Q. Pan, Y.H. Zhu, J.L. Wang, Z. Luo, L.M. Wang, X.D. Bai, F. Song, L.Z. Zhang, Y.B. Guo, Dual activation of molecular oxygen and surface lattice oxygen in single atom Cu_1/TiO_2 catalyst for CO oxidation, Angew. Chem. Int. Ed. 61 (2022), e202212273.

[28] L.Q. Kang, B.L. Wang, Q.M. Bing, M. Zalibera, R. Büchel, R.Y. Xu, Q.M. Wang, Y.Y. Liu, D. Gianolio, C.C. Tang, E.K. Gibson, M. Danaie, C. Allen, K. Wu, S. Marlow, L.D. Sun, Q. He, S.L. Guan, A. Savitsky, J.J. Velasco-Vélez, J. Callison, C.W.M. Kay, S.E. Pratsinis, W. Lubitz, J.Y. Liu, F.R. Wang, Adsorption and activation of molecular oxygen over atomic copper(I/II) site on ceria, Nat. Commun. 11 (2020) 4008.

[29] Y. Feng, L.Y. Dai, Z.W. Wang, Y. Peng, E.H. Duan, Y.X. Liu, L. Jing, X. Wang, A. Rastegarpanah, H.X. Dai, J.G. Deng, Photothermal synergistic effect of Pt_1/CuO–CeO_2 single-atom catalysts significantly improving toluene removal, Environ. Sci. Technol. 56 (2022) 8722–8732.

[30] X. Wang, L.K. Wu, Z.W. Wang, Y. Feng, Y.X. Liu, H.X. Dai, Z.H. Wang, J.G. Deng, Photothermal synergistic catalytic oxidation of ethyl acetate over MOFs-derived mesoporous N-TiO$_2$ supported Pd catalysts, Appl. Catal. B 322 (2023), 122075.

[31] K.L. Li, P. Chen, J.Y. Li, Y.J. Sun, Y.H. Chu, F. Dong, Enhanced plasmonic photocatalytic disinfection on noble-metal-free bismuth nanospheres/graphene nanocomposites, Catal. Sci. Technol. 8 (2018) 4600–4603.

[32] Y. Feng, P.J. Ma, Z.W. Wang, Y.J. Shi, Z.H. Wang, Y. Peng, L. Jing, Y.X. Liu, X. Wang, X.F. Zhang, J.G. Deng, H.X. Dai, Synergistic effect of reactive oxygen species in photothermocatalytic removal of VOCs from cooking oil fumes over Pt/CeO$_2$/TiO$_2$, Environ. Sci. Technol. 56 (2022) 17341–17351.

[33] P. Zhou, Y.G. Chao, F. Lv, K. Wang, W.Y. Zhang, J.H. Zhou, H. Chen, L. Wang, Y. J. Li, Q.H. Zhang, L. Gu, S.J. Guo, Metal single atom strategy greatly boosts photocatalytic methyl activation and C–C coupling for the coproduction of high-value-added multicarbon compounds and hydrogen, ACS Catal. 10 (2020) 9109–9114.

[34] W.B. Pei, Y.X. Liu, J.G. Deng, K.F. Zheng, Z.Q. Hou, X.T. Zhao, H.X. Dai, Partially embedding Pt nanoparticles in the skeleton of 3DOM Mn$_2$O$_3$: An effective strategy for enhancing catalytic stability in toluene combustion, Appl. Catal. B 256 (2019), 117814.

[35] X. Chen, S.C. Cai, E.Q. Yu, J.J. Li, J. Chen, H.P. Jia, Photothermo catalytic performance of ACo$_2$O$_4$ type spinel with light-enhanced mobilizable active oxygen species for toluene oxidation, Appl. Surf. Sci. 484 (2019) 479–488.

[36] Z.Y. Jiang, M.J. Tian, M.Z. Jing, S.N. Chai, Y.F. Jian, C.W. Chen, M. Douthwaite, L. R. Zheng, M.D. Ma, W.Y. Song, J. Liu, J.G. Yu, C. He, Modulating the electronic metal–support interactions in single-atom Pt$_1$–CuO catalyst for boosting acetone oxidation, Angew. Chem. Int. Ed. 61 (2022), e202200763.

[37] L.N. Chen, P. Verma, K.P. Hou, Z.Y. Qi, S.C. Zhang, Y.S. Liu, J.H. Guo, V. Stavila, M.D. Allendorf, L.S. Zheng, M. Salmeron, D. Prendergast, G.A. Somorjai, J. Su, Reversible dehydrogenation and rehydrogenation of cyclohexane and methylcyclohexane by single-site platinum catalyst, Nat. Commun. 13 (2022) 1092.

[38] H.F. Xiong, H.Y. Li, C.C. Du, D. Kunwar, G. Canning, A.K. Datye, D. Jiang, C. E. García-Vargas, X.I.P. Hernandez, Y. Wang, Q. Wan, S. Lin, S.C. Purdy, J. T. Miller, K. Leung, S.S. Chou, H.H. Brongersma, R.T. Veen, J.Y. Huang, H. Guo, Engineering catalyst supports to stabilize PdO$_x$ two-dimensional rafts for water-tolerant methane oxidation, Nat. Catal. 4 (2021) 830–839.

[39] L.K. Wu, J.G. Deng, Y.X. Liu, L. Jing, X.H. Yu, X. Zhang, R.Y. Gao, W.B. Pei, X. Q. Hao, A. Rastegarpanah, H.X. Dai, Pd/silicalite-1: An highly active catalyst for the oxidative removal of toluene, J. Environ. Sci. 116 (2022) 209–219.

[40] H. Gao, X.L. Lv, M. Zhang, Q. Li, J. Chen, Z.J. Hu, H.P. Jia, Copper-cobalt strong interaction to improve photothermocatalytic performance of cobalt-copper oxides supported on copper foam for toluene oxidation, Chem. Eng. J. 434 (2022), 134618.

[41] Z. Chen, Y. Peng, J.J. Chen, C.Z. Wang, H.B. Yin, H.M. Wang, C.F. You, J.H. Li, Performance and mechanism of photocatalytic toluene degradation and catalyst regeneration by thermal/UV treatment, Environ. Sci. Technol. 54 (2020) 14465–14473.

[42] T. Xiong, W.L. Cen, Y.X. Zhang, F. Dong, Bridging the *g*-C$_3$N$_4$ interlayers for enhanced photocatalysis, ACS Catal. 6 (2016) 2462–2472.

[43] H. Wang, Y.J. Sun, F. Dong, Insight into the overlooked photochemical decomposition of atmospheric surface nitrates triggered by visible light, Angew. Chem. Int. Ed. 61 (2022), e202209201.

[44] T.X. Zhou, P.F. Zhang, D.Q. Zhu, S.S. Cheng, H.J. Dong, Y. Wang, G.B. Che, Y. L. Niu, M. Yan, C.M. Li, Synergistic effect triggered by skeleton delocalization and edge induction of carbon nitride expedites photocatalytic hydrogen evolution, Chem. Eng. J. 442 (2022), 136190.

[45] U.J. Etim, P. Bai, O.M. Gazit, Z.Y. Zhong, Low-temperature heterogeneous oxidation catalysis and molecular oxygen activation, Catal. Rev. Sci. Eng. 65 (2023) 239–425.

[46] X. Zhang, Y.X. Liu, J.G. Deng, X.H. Yu, Z. Han, K.F. Zhang, H.X. Dai, Alloying of gold with palladium: An effective strategy to improve catalytic stability and chlorine-tolerance of the 3DOM CeO$_2$-supported catalysts in trichloroethylene combustion, Appl. Catal. B 257 (2019), 117879.

[47] Y. Feng, C.C. Wang, C. Wang, H.B. Huang, H.C. Hsi, E.H. Duan, Y.X. Liu, G.S. Guo, H.X. Dai, J.G. Deng, Catalytic stability enhancement for pollutant removal via balancing lattice oxygen mobility and VOCs adsorption, J. Hazard. Mater. 424 (2022), 127337.

[48] Q.H. Shang, N.F. Tang, H.F. Qi, S. Chen, G.L. Xu, C.T. Wu, X.D. Wang, Y. Cong, A palladium single-atom catalyst toward efficient activation of molecular oxygen for cinnamyl alcohol oxidation, Chin. J. Catal. 41 (2020) 1812–1817.

[49] J.L. Li, M. Zhang, Z.J. Guan, Q.Y. Li, C.Q. He, J.J. Yang, Synergistic effect of surface and bulk single-electron-trapped oxygen vacancy of TiO$_2$ in the photocatalytic reduction of CO$_2$, Appl. Catal. B 206 (2017) 300–307.

[50] F.C. Vallejo, D. Loffreda, M.T.M. Koper, P. Sautet, Introducing structural sensitivity into adsorption–energy scaling relations by means of coordination numbers, Nat. Chem. 7 (2015) 403–410.

[51] T.B. Li, F. Liu, Y. Tang, L. Li, S. Miao, Y. Su, J.Y. Zhang, H. Sun, M. Haruta, A. Q. Wang, B.T. Qiao, J. Li, T. Zhang, Maximizing the number of interfacial sites in single-atom catalysts for the highly selective, solvent-free oxidation of primary alcohols, Angew. Chem. Int. Ed. 57 (2018) 7795–7799.

[52] H.L. Yang, G.G. Li, G.X. Jiang, Z.S. Zhang, Z.P. Hao, Heterogeneous selective oxidation over supported metal catalysts: from nanoparticles to single atoms, Appl. Catal. B 325 (2023), 122384.

[53] J.Y. Li, X.A. Dong, G. Zhang, W. Cui, W.L. Cen, Z.B. Wu, S.C. Lee, F. Dong, Probing ring-opening pathways for efficient photocatalytic toluene decomposition, J. Mater. Chem. A 7 (2019) 3366–3374.

[54] X.H. Yu, J.G. Deng, Y.X. Liu, L. Jing, R.Y. Gao, Z.Q. Hou, Z.X. Zhang, H.X. Dai, Enhanced water resistance and catalytic performance of Ru/TiO$_2$ by regulating brønsted acid and oxygen vacancy for the oxidative removal of 1,2-dichloroethane and toluene, Environ. Sci. Technol. 56 (2022) 11739–11749.

[55] M.D. Smolikov, V.A. Shkurenok, L.I. Bikmetova, I.P. Prosvirin, T.I. Gulyaeva, A. V. Bukhtiyarov, E.A. Paukshtis, V.I. Bukhtiyarov, A.V. Lavrenov, Effect of hydrogen reduction and palladium promotion of tungstate-modified zirconia on isomerization of heptane, Mol. Catal. 529 (2022), 112527.